PLANETARY3D: A PHOTOGRAMMETRIC TOOL FOR 3D TOPOGRAPHIC MAPPING OF PLANETARY BODIES

Han Hu, Bo Wu *

Department of Land Surveying and Geo-Informatics, The Hong Kong Polytechnic University, Kowloon, Hong Kong - (han.hu, bo.wu)@polyu.edu.hk

Commission III, ICWG III/II

KEY WORDS: Planetary3D, Topographic Mapping, Bundle Adjustment, Dense Image Matching

ABSTRACT:

Planetary remote sensing images are the primary datasets for high-resolution topographic mapping and modeling of the planetary surfaces. However, unlike the mapping satellites for Earth observations, cameras onboard the planetary satellites generally present special imaging geometries and configurations, which makes the stereo photogrammetric process difficult and requires a large number of manual interactions. At the Hong Kong Polytechnic University, we developed a unified photogrammetric software system, namely Planetary3D, for 3D topographic mapping modeling of various planetary bodies using images collected by various sensors. Planetary3D consists of three modules, including: (1) the pre-processing module to deliver standardized image products, (2) the bundle adjustment module to alleviate the inconsistencies between the images and possibly the reference frame, and (3) the dense image matching module to create pixel-wise image matches and produce high quality topographic models. Examples of using three changeling datasets, including the MRO CTX, MRO HiRISE and Chang'E-2 images, have revealed that the automatic pipeline of Planetary3D can produce high-quality digital elevation models (DEMs) with favorable performances. Notably, the notorious jitter effects visible on HiRISE images can be effectively removed and good consistencies with the reference DEMs are found for the test datasets by the Planetary3D pipeline.

1. INTRODUCTION

Topographic information is essential to various planetary applications and science, including landing site selection (Wu et al., 2014), geomorphological and geological analysis (Jones et al., 2011), rover maneuvering (Qing et al., 2018), etc. In general, there are two major categories of datasets for topographic modeling, including the laser altimeter and high-resolution satellite images (HRSI) (Barker et al., 2016). The former has a remarkable higher vertical precision and global consistency (Di et al., 2012); however, in the horizontal direction, the strip-like points suffer from severe differences of density, which reduce the spatial resolution. On the other hand, the latter can provide much better spatial resolution and details (Robinson et al., 2010).

However, the workflow of photogrammetric processing of planetary satellite images is much more complex (Kirk et al., 2008) and we have yet to see an omnipotent solution for stereo processing of planetary satellite images. This is due to several key problems that such a solution needs to fulfill: camera geometry specification, bundle adjustment and dense image matching. Although some excellent frameworks have made such endeavors into this problem, such as ISIS3 (USGS, 2018), ASP[1] (Shean et al., 2016) and MICMAC[2] (Rupnik et al., 2017), we have found that it's quite possible that these solutions lack some core capabilities in the long pipeline, especially for mission specific problems. For examples, the HiRISE images consists of 10 separated CCDs (Li et al., 2011), which shares the same lens and could be merged into a single image to standardize the processing.

In order to make the procedure more straightforward and standard, we present Planetary3D, which aims to fill the gaps between raw images and the topographic models and produce standard datasets that could be consumed in other software. Firstly, the camera geometries of different platforms are converted to the Rational Polynomial Coefficients (RPCs) (Tao and Hu, 2002; Grodechi and Dial, 2003), which are agnostic to different planetary bodies and different camera intrinsic and exterior geometries. The images are also transformed into the standard format to be consumed in other software. Secondly, for multiple planetary satellite images, an integrated bundle adjustment (Wu et al., 2014) will remove the inter-image inconsistencies and try to fit globally with a global DEM, such as the DEM from LOLA (Lunar Orbiter Laser Altimeter) and MOLA (Mars Orbiter Laser Altimeter). The bundle adjustment estimates the affine correction in the image space, but are then converted to the standard RPC by refitting make the affine correction transparent to the end-users. At last the texture-ware SGM (Semi-Global Matching) (Hu et al., 2016) is responsible to produce the point clouds and interpolate the gridded DEM with corresponding resolution.

The rests of this paper are organized as the following. In the next section, we give a brief overview of related materials on camera geometry, bundle adjustment and dense image matching. Section 3 discusses each part of Planetary3D in more details and Section 4 shows some examples of the capabilities in producing DEMs for the Chang'E-2, MRO CTX and HiRISE images. Conclusion

* Corresponding author
[1]Ames Stereo Pipeline(ASP) is a photogrammetry suite developed by NASA Ames Centre (https://github.com/NeoGeographyToolkit/StereoPipeline)
[2] MICMAC is a photogrammetry software developed at IGN (https://micmac.ensg.eu/index.php/Accueil)

remarks, including the limitations and works for future directions, are given in the last.

2. RELATED WORKS

For planetary topographic mapping and modeling, two major sources of datasets are generally used, including the laser altimeter and HRSI. These datasets are complementary to each other in accuracy, coverage and spatial resolution and generally integrated (Wu et al., 2013). The laser altimeter can directly deliver stripped point clouds along the celestial meridian. Although the distance between each strip on the equator is relatively large, on the two pole areas, most strips intersect, which allows the global adjustment to provide a consistent spatial reference with high vertical accuracy (Di et al., 2012). On the other hand, the planetary satellite imagery is balanced in the spatial resolution and generally much more detailed.

However, the geometrical modeling of the camera, including the definition of the focal plane and exterior orientation parameters, is much more cumbersome. As a hindsight to our previous works (Wu et al., 2014; Hu and Wu, 2018), we have found that the focal planes are different from mission to mission and even different camera sensors on the same platform, e.g. NAC-L and NAC-R onboard LRO are different (Robinson et al., 2010), CTX and HiRISE onboard MRO are different (Malin et al., 2007; McEwen et al., 2007). Although the rigorous camera model in ISIS3 (USGS, 2018) is capable to solve this problem, it involves three separated maps among ground, physical focal plane, undistorted focal plane, and digital CCD number. The partial derivatives for these maps are hard to generate analytically. In fact, approximate camera models for pushbroom sensors, such as RPC (Grodechi and Dial, 2003), are also widely used in photogrammetry processing of HRSI and the approximate errors are negligible for state-of-the-art satellite platforms, as investigated in the work by Tao and Hu (2002). RPC is agnostic to the complex geometry and analytically differentiable. In addition, there is no overhead using the reverse RPC for space intersection (Tao and Hu, 2002), if not faster than the iterative projection caused by the polynomial coefficients of exterior orientation parameters. Therefore, in Planetary3D, RPC is fitted for photogrammetric processing.

Unlike the 3D points measured by laser altimeters, the inconsistencies between different images are specific to different sensors and harder to be modeled. For example, the HiRISE image consists of many separated CCDs assembled on the same focal plane and 10 red CCDs can be used for topographic mapping (McEwen et al., 2007). Kirk et al. (2008) have analyzed the arrangement of all the CCDs, gives the affine parameters with respect to the focal plane and implements the transformation in the *noproj* routine of ISIS3. We have found that occasionally, gaps between different CCD are still observable and in Planetary3D, a special focal plane adjustment is used to fix this issue. For CTX and HiRISE, they are on board the same platform, the boresight offsets between them may also be interesting for topographic mapping of Mars (Wang and Wu, 2017). Furthermore, the alignment between image matches and the reference frame, generally DEM from laser altimeter data, should also be considered. Profile analysis (Henriksen et al., 2017) and direct point clouds registration in ASP are two possible solutions and in the proposed framework, this issues is directly considered in the combined adjustment with DEM (Wu et al., 2014).

The dense image matching is also a classic but non-trivial problem for stereo processing. Traditional methods generally use correlation as similarity measurements and the winner-take-all strategy in a local window to find the best matches (Wu et al., 2011). However, local methods suffer ambiguities from the repeated pattern and textureless areas, and therefore global methods (Scharstein and Szeliski, 2002) are preferred. The industrial proved SGM (Hirschmuller, 2008) has recently been implemented and extended in many systems including ASP, MICMAC and some other commercial software packages. In Planetary3D, an extension of SGM (Hu et al., 2016) using ternary census transform and texture information is used as the backend for dense image matching.

3. THE INTEGRATED PHOTOGRAMMETRIC FRAMEWORK OF PLANETARY3D

Planetary3D consists of three main modules, including the pre-processing, bundle adjustment and dense image matching. The first module mainly converts the images from different missions into the standard product with an RPC file for georeferencing, and occasionally mission-specific pre-processing is also considered. The second module takes the normalized images and refines the RPC with an affine correction in the image space; the corrections are refitted into the RPC to retain the products standard. The last part rectifies the stereo image pair to the horizontal epipolar space and conducts an improved SGM to obtain the disparity image; furthermore, point clouds and gridded terrain model are also generated.

3.1 Normalization of images based on ISIS3

3.1.1 Generation of RPC parameters

Because the camera geometry changes for different platforms and sensors, in order to unify the processing, all the images are attached with an RPC file before successive processing. This step is built on the ISIS3 library. Specifically, after initializing the image with the SPICE kernels either locally from the kernel data or remotely from the web services, we can obtain a one-on-one map between the image pixels and the geographic ground coordinate. The ground point is the intersection between the ray defined by the image pixel and the terrain model, which could be either a DEM or simply an ellipse of the target planet.

The RPC fitting is slightly different from the standard way (Grodechi and Dial, 2003) as shown in Figure 1a. The standard RPC fitting method first determines the minimum and maximum height in the areas covered by the image and generate several virtual ground control points from several uniformly distributed planes. These virtual ground control points are projected to the image space using the rigorous sensor models (e.g. the polynomial model). Then the 3D point on the virtual plane and 2D pixel coordinates are used to fit the RPCs by least-squares optimization. However, if the image is too long and the terrain height varies significantly, it's possible that the 3D points may not successfully project onto the image. Therefore, in Planetary3D, the height of the virtual GCPs are generated according to the ground points, as shown in Figure 1b.

RPC defines the projective relationship $\mathbf{\Pi}$ between a 3D point in the object space $\boldsymbol{X} = (\lambda, \phi, h)^T$ and the 2D point in the image space $\boldsymbol{p} = (s, l)^T$ as $\boldsymbol{p} = \mathbf{\Pi}(\boldsymbol{X})$. However, for space intersection, this formulation requires time-consuming iterative solutions to solve the 3D point. Therefore, the reverse RPCs are also fitted using a similar procedure as described in Figure 1. The reverse RPC defines the back-projection $\mathbf{\Pi}'$ of the image point and the corresponding height $\boldsymbol{p}' = (s, l, h)^T$ to the 2D horizontal coordinate $\boldsymbol{X}' = (\lambda, \phi)^T$ as $\boldsymbol{X}' = \mathbf{\Pi}'(\boldsymbol{p}')$. For space intersection, the height h of the 3D point $\boldsymbol{X}$ is solved first using the reversed

This contribution has been peer-reviewed. The double-blind peer-review was conducted on the basis of the full paper.
https://doi.org/10.5194/isprs-annals-IV-2-W5-519-2019 | © Authors 2019. CC BY 4.0 License.

RPC and then get $\boldsymbol{X}'$ directly (Tao and Hu, 2002). In addition, the reverse RPC is generated in runtime when required.

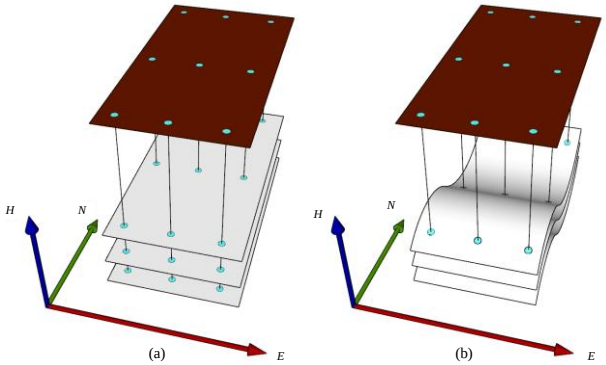

Figure 1. (a) The standard RPC fitting method generates the virtual ground control points from uniformly distributed horizontal planes between the height range. (b) The proposed RPC fitting method in Planetary3D generates the points according to the terrain surface. This will improve the fitting performance when the image covers a vast area and the height is spanning a large interval.

Another important issue in the fitting of RPC parameter is to suppress the high-frequency vibration of the high order parameters, e.g. the 6 second-order and 10 third-order parameters for all the denominators and numerators (Hartley and Saxena, 2001). An intuitive interpretation of this is that: 1) The projective camera geometry, formulated as co-linear equation (Wang, 1990), has only first-order parameters; 2) The RPCs with 78 adjusted parameters generally over-fit the pushbroom sensors and therefore are not stable, regularization should be applied. Specifically, the rational coefficients $(\boldsymbol{c}^T, \boldsymbol{d}^T, \boldsymbol{e}^T, \boldsymbol{f}^T)$ (Grodechi and Dial, 2003) in the RPC model $\boldsymbol{\Pi}$ are estimated in the following regularized least-squares optimization,

$$\min_{\boldsymbol{c},\boldsymbol{d},\boldsymbol{e},\boldsymbol{f}} \frac{(1-\lambda)}{|Z|}\sum_i \left\| w_p\left(\boldsymbol{p}_i - \boldsymbol{\Pi}(\boldsymbol{X}_i)\right)\right\|^2 + \frac{\lambda}{80}\|\boldsymbol{w}_r^T\boldsymbol{c} + \boldsymbol{w}_r^T\boldsymbol{d} + \boldsymbol{w}_r^T\boldsymbol{e} + \boldsymbol{w}_r^T\boldsymbol{f}\|^2 \quad (1)$$

where λ balances the importance of pixel projection accuracy and the regularization term in the second row and $\lambda = 0.5$ is fixed during experiments. w_p and $\boldsymbol{w}_r$ are the weights for pixel projection and regularization, respectively, and both of them are determined by the inverse of a priori standard deviation; in general, 0.01 pixels and 10^{-5} are set for the standard deviation values. $|Z|$ is the total number of pixel values used for normalization.

3.1.2 Radiometric and geometric pre-processing

The input images generally incorporate some radiometric defects, for example, the digital number may not scale linearly to the real value, each column on the CCD sensor may not be consistent and for some applications radiance rather than the value of digital number is preferred. Therefore, radiometric calibration is also a fundamental step for further application. We use the binary executables provided by ISIS3 to conduct the radiometric calibration. In addition, after calibration, the images are generally encoded and quantized with a 32-bit floating number. This is unnecessarily high for image matching, and therefore after calibration, the images are then converted to an 8-bit integer in the range of [1, 255] by truncating the pixels smaller or larger than a certain percent (0.5% is used) and value 0 indicates invalid pixels.

Although for most images, after the above radiometric calibration, the products can be directly consumed by the following steps, this is not the case for MRO HiRISE images. A single HiRISE image consists of 10 CCDs and 20 EDR products. And the standard processing pipeline using ISIS3 still leaves us with 10 undistorted images (Kirk et al., 2008), with the same camera geometry. Because small uncompensated displacement of the CCDs, direct merging of the images will sometimes cause obvious jitter effect in the DEM. Because the overlap between adjacent CCDs is only 24 pixels (McEwen et al., 2007) and 12 pixels in the down-sampling case, general feature matching method is not capable of handling this scenario, for instance, SIFT (Lowe, 2004) requires 64 pixels to compute the descriptor. Therefore, the normalized correlation coefficient of uniformly distributed corners is searched and filtered in a small window (7 pixels and threshold of 0.9). The matches are used to estimate a four-parameter rotation model, e.g. $x' = ax + by + c, y' = -bx + ay + d$ for each image and the center image is kept fixed. All the images are then merged sequentially to the output and graph cut is used to smooth the seam line (Kwatra et al., 2003).

3.2 Multi-image bundle adjustment

The bundle adjustment has three practical effects in the topographic modeling of planetary images: 1) To remove the vertical disparity after epipolar rectification, this is important for image matching using SGM, because only horizontal disparity is considered; 2) To remove the inconsistencies between multiple stereo pairs, for example, stereo pairs of MRO CTX from multiple orbits, as shown in Section 4.2; 3) To enforce consistency with the reference frame, such as DEM from laser altimeter data, either from control points or the combined bundle adjustment (Wu et al., 2014). In the following, we demonstrate the methods used in Planetary3D for an automatic and robust bundle adjustment of multiple images under extremely difficult conditions.

3.2.1 Feature matching in low overlapping regions

Unlike the structured aerial photogrammetry that may have up to 90% overlap for adjacent images, the stereo pairs of planetary HRSI generally prefer enlarging the coverage to the multi-view capability. Therefore, for different stereo pairs, it's quite possible that only small parts of the images overlap. If all the feature descriptors in the whole image are compared, the search space may be too large to recall enough feature matches. In addition, the planetary terrain surface features textureless pattern, which further decreases the performance of feature descriptors.

In order to improve the performance of feature matching, the corresponding RPCs are used to guide the image matching. As shown in Figure 2, the RPCs and reverse RPCs are used to project and back-project the image point $\boldsymbol{p}$ to the other image as $\boldsymbol{p}'$. $\boldsymbol{p}'$ is visible if it is inside the other image within a buffer d and only mutually visible features for a stereo pair are considered for descriptor comparison. In addition, because the overlap region is irregular, which may cause the RANSAC (Random Sample Consensus) outlier removal not robust, therefore no RANSAC is used, but the distance threshold d is used to test if $(\boldsymbol{p}, \boldsymbol{q})$ is a valid match. For multiple images, all the image pair are exhausted and pairwise matches are connected to longer match track using connected components (Agarwal et al., 2011).

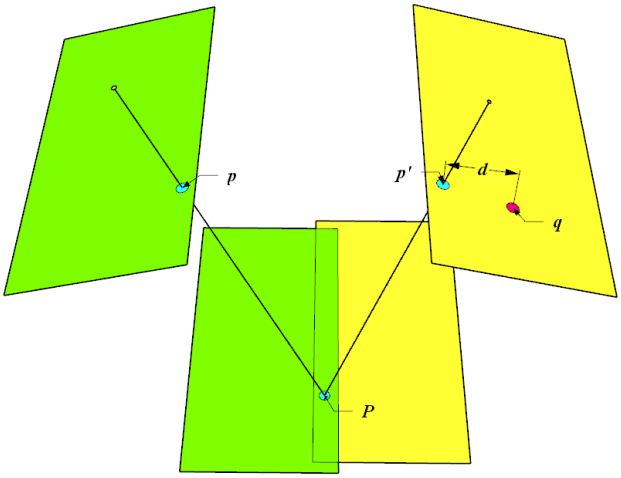

Figure 2. Robust image matching in the low overlap region. Visibility is defined by back-projecting the point $\boldsymbol{p}$ from the one image to the object space $\boldsymbol{P}$ and then project to the second image $\boldsymbol{p}'$. Only mutually visible features (with a buffer distance of d) are considered for pairwise descriptor comparisons. Because RANSAC is not robust when the overlapping area is thin and narrow, the distance threshold d is also responsible to test if a match $(\boldsymbol{p}, \boldsymbol{q})$ is valid.

3.2.2 Integrated bundle adjustment with laser altimeter data

The inputs to the integrated bundle adjustment is a set of match tracks $\mathbf{T} = \{t_i | \boldsymbol{X}_i, (\dots \boldsymbol{p}_{ij} \dots)\}$, where the i-th match track t_i contains an unknown 3D point $\boldsymbol{X}_i$ and multiple (at least two) image points $\boldsymbol{p}_j$ (j is the image index). Optionally, a reference DEM using the laser altimeter data, such as MOLA DEM or LOLA DEM, can also be used, from which a set of height observations can be sampled from the DEM using the initial 3D point $\boldsymbol{X}_i$ as $\boldsymbol{H} = \{\hat{h}_i | i = 1,2 \dots\}$. The optimization targets of the integrated bundle adjustment are a set of affine parameters in the image space, $\mathbf{M} = \{\mathbf{M}_j | (\boldsymbol{A}_j, \boldsymbol{b}_j), j = 1,2 \dots\}$ for each image j. The combined bundle adjustment models the following least-squares problem.

$$\min_{\mathbf{M},\boldsymbol{X}} \frac{\lambda_p}{|Z|} \sum_{i,j} \left(\boldsymbol{w}_p \left(\mathbf{M}_i \boldsymbol{\Pi}_i (\boldsymbol{X}_j) - \boldsymbol{p}_{ij} \right) \right)^2 + \frac{\lambda_h}{|H|} \sum_i \left(w_h \left(h_i - \hat{h}_i \right) \right)^2 + \frac{\lambda_m}{|M|} \sum_j \left\| \mathbf{w}_M \left(\mathbf{M}_j - \mathbf{I} \right) \right\|_F^2 \quad (2)$$

In Equation (2), $|Z|, |H|, |M|$ are the normalization factor for each observation, e.g. the number of all the summations; $\boldsymbol{w}_p, w_h$ and $\mathbf{w}_M$ are the weights for image pixel, DEM height and initial affine parameters, respectively, the weights are determined by the inverse of the *a priori* precision; λ is a balancing factor between all the three terms and are generally kept fixed as $\lambda_p = 0.9, \lambda_h = 0.05$ and $\lambda_m = 0.05$, which award the image pixel observations the largest priority to obtain inter-image consistency; And $\mathbf{I}$ is the identity affine transformation as $\mathbf{I} = \begin{pmatrix} 1 & 0 & 0 \\ 0 & 1 & 0 \end{pmatrix}$. Unlike our previous work (Wu et al., 2014), in which the DEM constraint is formulated as the distance to the body center, because for RPC the 3D points are in the geographic coordinate system, the height value can be used directly.

Because outliers are inevitable in image matching, especially that no RANSAC paradigm is employed, the outliers should be properly handled in the bundle adjustment procedure. Therefore, the 68–95–99.7 law is used to remove outliers. We first evaluate the residuals of the first term in Equation (2) and compute σ_0 from the residuals, if a single residual of the track t_i exceeds $3\sigma_0$, the whole track is removed from bundle adjustment. In addition, the corresponding DEM constraints are also omitted. The bundle adjustment iterates several times, until no more outliers are detected or reach the maximum number of iterations (10 is used). The least-squares optimization in Equation (2) can be efficiently solved using the Ceres Solver provided by Google Inc. (Agarwal and Mierle, 2010).

After the bundle adjustment, the projection of 3D geographic coordinates has been redefined as $\boldsymbol{p} = \mathbf{M}\boldsymbol{\Pi}(\boldsymbol{X})$, which violates the standard format. In order to make the image products consumable in other software, the affine transformation $\mathbf{M}$ is refitted into the RPC parameters $\boldsymbol{\Pi}$. This is similar to the generation of the RPC file, except that the pixel coordinates are obtained using $\boldsymbol{p} = \mathbf{M}\boldsymbol{\Pi}(\boldsymbol{X})$ rather than the intrinsic and exterior orientation parameter from the SPICE kernel. The reason to use "*affine correction + RPC refitting*" rather than "*direct RPC correction*" (Wu et al., 2015) is that the weights are much easier to define for the affine matrix $\mathbf{w}_M$ than those of the RPC coefficients, which has no physical significance. In addition, the six affine parameters are already abundant to correct the errors, while the 78 RPC coefficients may suffer the severe problem of overfitting. After the refitting of RPC using the affine transformation, the reverse RPC is also generated from the updated data.

3.3 Dense image matching

3.3.1 Epipolar rectification

Before dense image matching, epipolar rectification is required to remove the vertical disparity. Unlike the frame camera, the epipolar geometry for pushbroom satellite image is, in theory, a hyperbola rather than a straight line. However, it is widely known that, for HRSI, the epipolar geometry could be approximated by affine or homographic transformation (Wang et al., 2011; Jannati et al., 2018). Similar to the ASP (Shean et al., 2016), we also use affine transformation in the object space. The affine transformation implicitly assumes that all the epipolar lines in one image are parallel. Figure 3 illustrates the methods to trace a single epipolar curve. Beginning with a point on one image p_1 and the highest and lowest plane defined by the RPC parameter, this point is iteratively projecting and back-projecting to the image and object space, respectively. This will generate half of the epipolar curve as (p_1, p_2, p_3) and by changing the first point from the highest plane to the lowest plane, the epipolar line will march towards the opposite direction.

Because the geographic coordinate system has unbalanced latitude and longitude units, e.g., a degree does not mean the same distance for latitude and longitude, the epipolar curve $\boldsymbol{l} = \{\boldsymbol{p}_1, \boldsymbol{p}_2, \dots\}$ is projected to the Mercator coordinate system with reference meridian and center of latitude at the center of the image. This will remove the distortion caused by the geographic coordinate system, and thus is dependent to the planetary body. The rectified image is resampled with each scanline parallel to the epipolar line on the Mercator coordinate system.

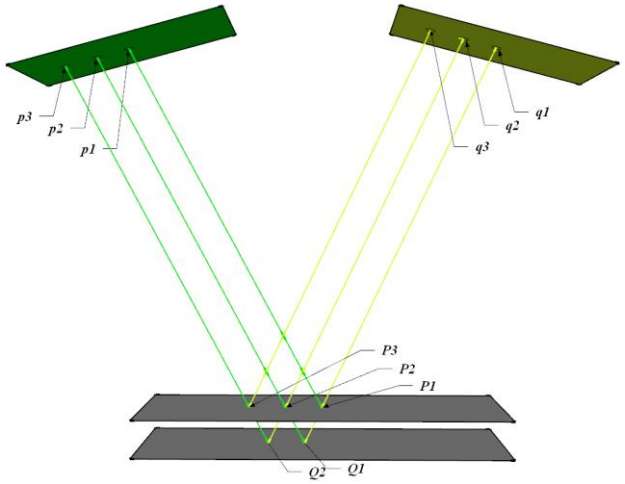

Figure 3. Tracing the approximate epipolar line using RPC information by alternatively project and back-project points between a stereo pair. The sequence generated by this step in the figure above is $(p_1 \rightarrow P_1 \rightarrow q_1 \rightarrow Q_1 \rightarrow p_2 \rightarrow P_2 \rightarrow q_2 \rightarrow Q_2 \rightarrow p_3 \rightarrow P_3)$.

3.3.2 Texture-aware semi-global matching

SGM extends the dynamic programming from a single scanline to multiple paths, which alleviate the inconsistent disparity along the vertical direction (Scharstein and Szeliski, 2002). Other than the 2D Markov Random Field on lattice grid, dynamic programming on a 1D scanline can be solved in polynomial time and SGM also inherits this merit. Many industrial proved software solutions have implemented SGM. In Planetary3D, the texture-aware SGM is used and the ternary census transform is chosen for matching cost because it can improve the distinctiveness on textureless areas. Please refer to the following references for more implementation details (Hirschmuller, 2008; Rothermel et al., 2012; Hu et al., 2016).

In SGM, although vertical disparity can be considered by implementation tricks, however, this will significantly increase the search space of disparity range, especially that SGM already consumes a lot of memory, which is related to the disparity search space. In addition, only parabola fitting by adjacent three disparity values is used for subpixel localization, which may lead to undesired results in textureless regions. Therefore, the least-squares matching is used to refine the valid matches in the disparity map. In order to accelerate the least-squares matching, a parallel implementation using the Graphics Computing Unit (GPU) based on OpenCL is used in Planetary3D and based on our empirical experiment, the GPU implementation is an order of magnitude faster than the CPU counterpart.

4. EXPERIMENTAL EVALUATIONS

Most of the core functionalities of Planetary3D are implemented in C++, with some pipelines invoked from Python. In the following, we demonstrate the whole photogrammetric pipeline from the PDS EDR data to the final gridded DEM using three datasets, i.e., the Chang'E-2 images (Wu et al., 2014) for the Moon, and the MRO CTX (Malin et al., 2007) and MRO HiRISE (McEwen et al., 2007) images for Mars. Performances of Planetary3D for photogrammetric processing of the LROC NAC images can be referred in our previous publications (Wu and Liu, 2017; Hu and Wu, 2018)

4.1 Chang'E-2 Images

Chang'E-2 has a two-line pushbroom stereo sensor onboard, which has a convergent angle of approximately 25° and collects stereo image in a single orbit. The Chang'E-2 satellite flew at two different types of orbits and captures images at two different resolutions, including the circular orbit for 7 *m* images and the elliptical orbit for 1.5 *m*. The initial EO parameters of the Chang'E-2 images are not provided in the SPICE format and therefore, we have made another routine to extract the RPC parameters for the Chang'E-2 images and convert the original image format (the PDS3) to the standard GeoTIFF format. For detailed specifications of the Chang'E-2 images, we refer the readers to our previous work (Wu et al., 2014).

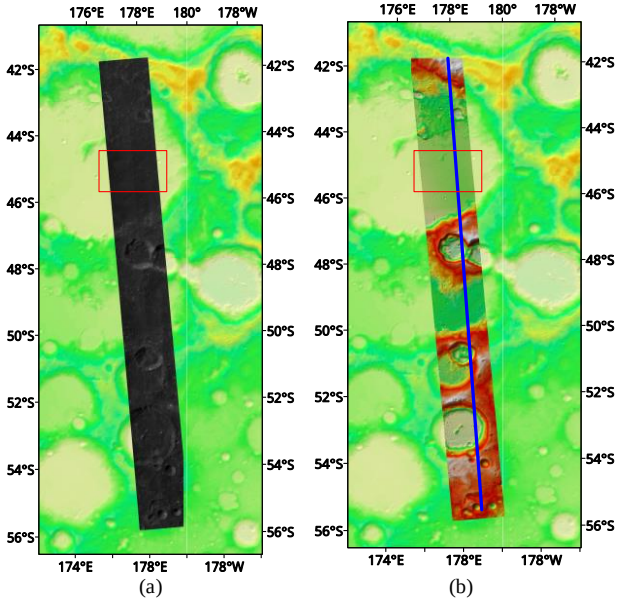

Figure 4. The forward view of the stereo pair (a) and the generated DEM (b) from orbit 0392 overlaid on the SLDEM (Barker et al., 2016). The blue line indicates the profile in Figure 5. The white gap is the artifacts caused by the rendering software ESRI ArcMap around the antimeridian of the moon.

In this paper, we used a pair of stereo images from the orbit 0392 of Chang'E-2 satellite as shown in Figure 4a, which cover the landing site of the Chang'E-4 mission (red box) in the Von Kármán crater and has a spatial resolution of 7 *m*. Because of different reference frames, we have seen relatively large horizontal offsets between the Chang'E-2 image and the SLDEM, which is the new standard global terrain model by registration of different sources (Barker et al., 2016). Therefore, for Chang'E-2 DEM processing, a free network adjustment is applied to avoid imposing constraints on the DEM, otherwise, the height samples from the DEM may deviate too much for the correct position. After the adjustment and dense image matching, Figure 4b demonstrates the obtained terrain model at the spatial resolution of 20 *m*.

The blue line in Figure 4b indicates the position of the profile comparison between Chang'E-2 DEM and SLDEM, as shown in Figure 5. It could be noticed that the area is a large plain formulated after the impact. However, except for the Chang'E-4 landing site, the height variation of other areas is very severe. In addition, we could also notice the systematic difference between the two DEMs, in both vertical and horizontal directions. However, because the differences are consistent along the entire

profile, it's quite possible for using only a few ground control points to correct the differences.

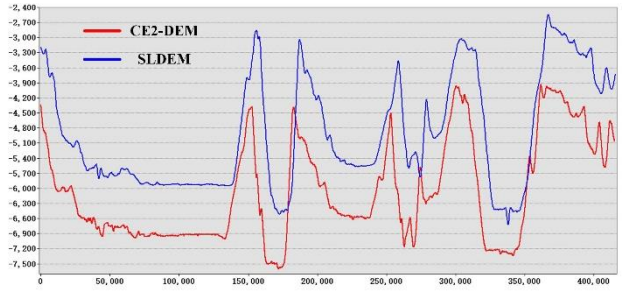

Figure 5. Profile comparison between the Chang'E-2 DEM and SLDEM.

4.2 MRO CTX Images

For the MRO CTX datasets, three pairs of CTX images are selected, including (1) G01-018543-1992 and G03-019255-1992, (2) F01-036107-1982 and F23-044705-1982, (3) D02-028169-1989 and G22-026758-1988. The coverage areas of each stereo pair are shown in Figures 6 and 7, where each image is abbreviated by the first three letters, and it should be noted that the overlap region between pair F01-F23 and pair G01-G03 is only less than 300 pixels, compared to about 5,000 samples of CTX image. Although the other overlap region is relatively larger, compared to the scope of the whole area of D02-G23, the overlap region is still less than 10%. The CTX images have spatial resolutions of 6 m/pixel, and DEMs of 20 m resolution are generated using the Planetary3D pipeline.

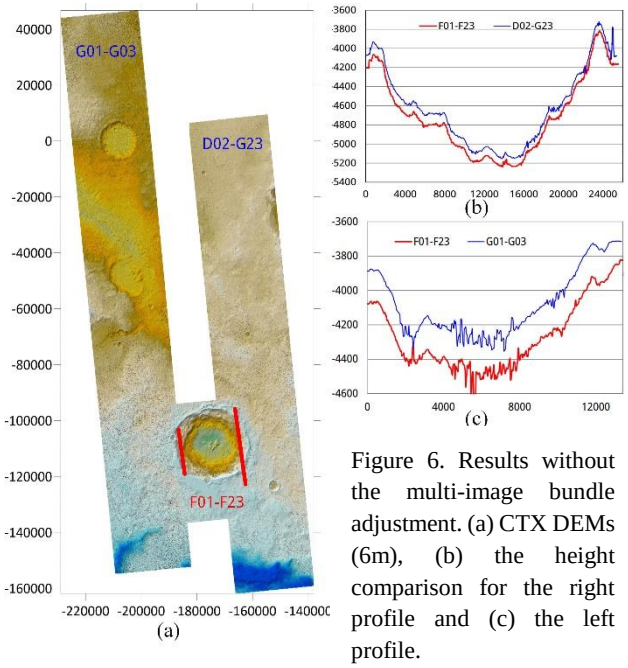

Figure 6. Results without the multi-image bundle adjustment. (a) CTX DEMs (6m), (b) the height comparison for the right profile and (c) the left profile.

In order to test the performances of the integrated bundle adjustment, two sets of DEMs are generated, with and without the integrated bundle adjustment. Two profiles along the overlap regions are selected, it could be noted that without the multi-image bundle adjustment, the inconsistencies between the profiles could be larger than 200 m and present obvious systematic offsets between the two DEMs. But after the bundle adjustment, the discrepancies have been satisfactorily removed, even for the extreme low overlap ration between F01-F23 and G01-G03 as shown in Figure 7c. This has proved that the proposed image matching strategy is efficient in recalling enough number of feature match tracks with multiple tie-points in this narrow overlap region.

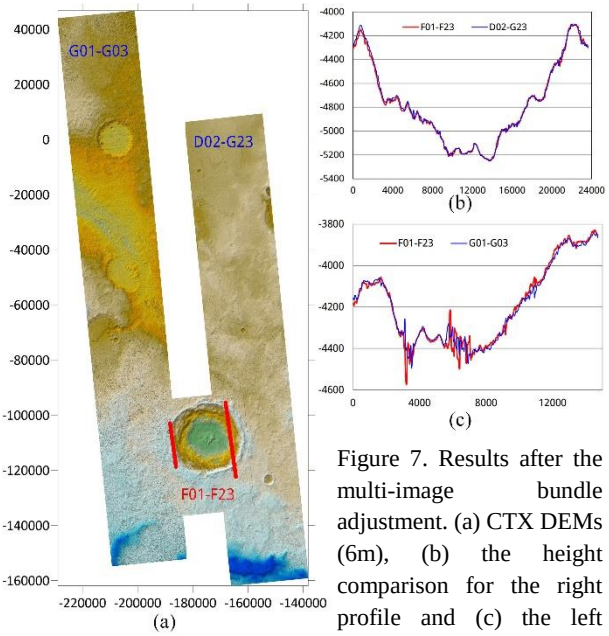

Figure 7. Results after the multi-image bundle adjustment. (a) CTX DEMs (6m), (b) the height comparison for the right profile and (c) the left profile.

4.3 MRO HiRISE Images

HiRISE and CTX are onboard the same satellite platform and collect stereo image pairs by rolling the satellite in another track. In order to reach a high spatial resolution (typically 0.3 m/pixel) on the ground, HiRISE has a focal length of about 12 m and because it is still hard to engineer large frame CCD, a series of CCDs are assembled almost parallel on the focal plane, in which each CCD has 2048 samples and about 48 pixels' overlap. Among them, 10 CCDs capturing the red band can be mosaicked together to formulate a single image with the same physical camera geometry. The mosaicking parameters are calibrated as presented in the pioneering work by Kirk et al. (2008) on the photogrammetric processing of HiRISE stereo pairs.

This mosaic pipeline is implemented in ISIS3, by sequentially applying several routines, including *hi2isis*, *hical*, *histich*, *spiceinit*, *noproj*, *hijitreg* and *handmos*. However, even after the above processing pipeline, obvious jitter effects can be still found in the generated DEMs occasionally. This problem is possibly caused by a failure in feature matching and mosaic when no matches are found *hijitreg* and *handmos* only considers integer coordinate offset and no seam-line fusion is used. Therefore, the undistorted images from *noproj* are used and merged in Planetary3D as described previously.

A HiRISE stereo pair, including ESP-029716-1980 and ESP-029426-1980 covering the source area for channel network near Gigas Sulci, is selected to test the performance of Planetary3D, and a DEM of 1 m resolution is generated. The DEM on the website of the vendor[3] is also obtained for comparison, denoted as AU in below. In addition, the pipeline with *hijitreg* and

[3] https://www.uahirise.org/dtm/

handmos, taken from ASP is also used for stereo matching, denoted as ASP. Figure 8 shows the overall view of the three DEMs. It should be noted that the datum for both ASP and Planetary3D are the spherical Mars model, which is used in ISIS3. Therefore, the datum is different from the DEM by AU. The jitter patterns on some CCD regions are clearly observed for both ASP and AU. However, the jitter effects have been satisfactorily compensated by Planetary3D. The same effect is clearer in the enlarged view of the channel area, as shown in Figure 9.

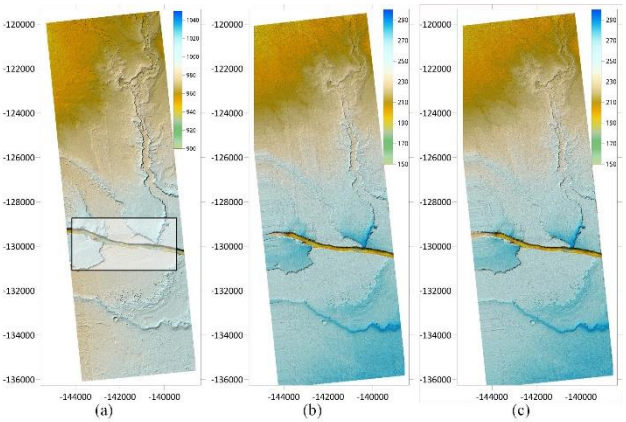

Figure 8. Comparison of DEM in the channel areas. (a) AU, (b) ASP and (c) Planetary3D. It should be noted that DEM from AU has a different datum, therefore the height range and color scale are different from those of ASP and Planetary3D. The rectangle indicates the enlarged area in Figure 9.

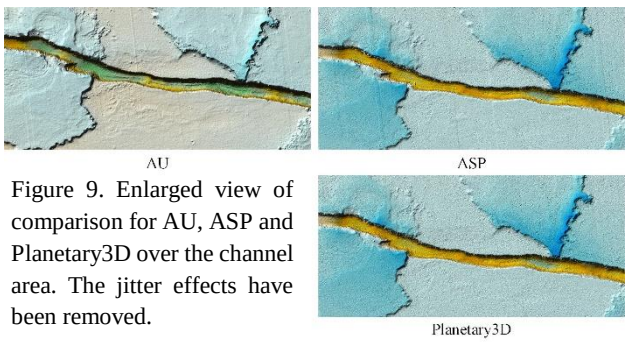

Figure 9. Enlarged view of comparison for AU, ASP and Planetary3D over the channel area. The jitter effects have been removed.

5. CONCLUSIONS

This paper presents the Planetary3D, a software pipeline to unify the photogrammetric processing of planetary satellite images. The basic idea is to transform the planetary images, with peculiar camera geometries, stereo formulation, into standard formats with the RPC files. The standardized products can be consumed in a uniform way for bundle adjustment and dense image matching in Planetary3D, or in other commercial photogrammetric solutions. We have shown three challenging examples for Chang'E-2, MRO CTX, and HiRISE images, which features low overlapping and unusual image geometry. The performances are on par with, if not even better than, the vendor provided reference DEM that requires cumbersome manual interactions.

Planetary3D can be further extended to process images from planetary bodies other than the Moon and Mars. It offers another solution for image-based planetary topographic mapping in addition to the existing solutions.

ACKNOWLEDGEMENTS

This work was supported by a grant from the Research Grants Council of Hong Kong (Project No. 152086/15E) and grants from the National Natural Science Foundation of China (Project No. 41471345 and 41671426). We would like to extend our appreciations to the institutes and persons, for making the datasets and ISIS3 publicly available, which has set the foundation of this research.

REFERENCE

Agarwal, S., Furukawa, Y., Snavely, N., Simon, I., Curless, B., Seitz, S.M., Szeliski, R., 2011. Building Rome in a day. *Communications of the ACM*, 54 (10), 105-112.

Agarwal, S., Mierle, K., 2010. Ceres Solver, http://ceres-solver.org/. (30 August, 2016)

Barker, M.K., Mazarico, E., Neumann, G.A., Zuber, M.T., Haruyama, J., Smith, D.E., 2016. A new lunar digital elevation model from the Lunar Orbiter Laser Altimeter and SELENE Terrain Camera. *Icarus*, 273, 346-355.

Di, K., Hu, W., Liu, Y., Peng, M., 2012. Co-registration of Chang' E-1 stereo images and laser altimeter data with crossover adjustment and image sensor model refinement. *Advances in Space Research*, 50(12), 1615-1628.

Grodechi, J., Dial, G., 2003. Block adjustment of high-resolution satellite images described by rational polynomials. *Photogrammetric Engineering and Remote Sensing*, 69 (1), 59-68.

Hartley, R.I., Saxena, T., 2001. The cubic rational polynomial camera model. Image Understanding Workshop, Palo Alto, California, USA.

Henriksen, M.R., Manheim, M.R., Burns, K.N., Seymour, P., Speyerer, E.J., Deran, A., Boyd, A.K., Howington-Kraus, E., Rosiek, M.R., Archinal, B.A., 2017. Extracting accurate and precise topography from LROC narrow angle camera stereo observations. *Icarus*, 283, 122-137.

Hirschmuller, H., 2008. Stereo processing by semiglobal matching and mutual information. *IEEE Transactions on Pattern Analysis and Machine Intelligence*, 30 (2), 328-341.

Hu, H., Chen, C., Wu, B., Yang, X., Zhu, Q., Ding, Y., 2016. Texture-Aware Dense Image Matching using Ternary Census Transform. *ISPRS Annals of the Photogrammetry, Remote Sensing and Spatial Information Sciences*, III-3, 59-66. doi.org/10.5194/isprs-annals-III-3-59-2016

Hu, H., Wu, B., 2018. Block Adjustment and Coupled Epipolar Rectification of LROC NAC Images for Precision Lunar Topographic Mapping, *Planetary and Space Science*, 160, 26-38.

Jannati, M., Valadan Zoej, M.J., Mokhtarzade, M., 2018. A novel approach for epipolar resampling of cross-track linear pushbroom imagery using orbital parameters model. *ISPRS Journal of Photogrammetry and Remote Sensing*, 137, 1-14.

Jones, A.P., McEwen, A.S., Tornabene, L.L., Baker, V.R., Melosh, H.J., Berman, D.C., 2011. A geomorphic analysis of

Hale crater, Mars: The effects of impact into ice-rich crust. *Icarus*, 211, 259-272.

Kirk, R.L., Howington Kraus, E., Rosiek, M.R., Anderson, J.A., Archinal, B.A., Becker, K.J., Cook, D.A., Galuszka, D.M., Geissler, P.E., Hare, T.M., 2008. Ultrahigh resolution topographic mapping of Mars with MRO HiRISE stereo images: Meter‐scale slopes of candidate Phoenix landing sites. *Journal of Geophysical Research: Planets*, 113 (E3).

Kwatra, V., Schödl, A., Essa, I., Turk, G., Bobick, A., 2003. Graphcut textures: image and video synthesis using graph cuts. *ACM Transactions on Graphics*, 22 (3), 277-286.

Li, R., Hwangbo, J., Chen, Y., Di, K., 2011. Rigorous Photogrammetric Processing of HiRISE Stereo Imagery for Mars Topographic Mapping. *IEEE Transactions on Geoscience and Remote Sensing*, 49 (7), 2558-2572.

Lowe, D.G., 2004. Distinctive image features from scale-invariant keypoints. *International Journal of Computer Vision*, 60 (2), 91-110.

Malin, M.C., Bell, J.F., Cantor, B.A., Caplinger, M.A., Calvin, W.M., Clancy, R.T., Edgett, K.S., Edwards, L., Haberle, R.M., James, P.B., 2007. Context camera investigation on board the Mars Reconnaissance Orbiter. *Journal of Geophysical Research: Planets*, 112 (E5).

McEwen, A.S., Eliason, E.M., Bergstrom, J.W., Bridges, N.T., Hansen, C.J., Delamere, W.A., Grant, J.A., Gulick, V.C., Herkenhoff, K.E., Keszthelyi, L., 2007. Mars reconnaissance orbiter's high resolution imaging science experiment (HiRISE). *Journal of Geophysical Research: Planets*, 112 (E5).

Qing, M.Y., Chuang, L.S., Bo, W., Shuo, Z., Lei, L.M., Song, P., 2018. Weighted Total Least Squares for the Visual Localization of a Planetary Rover. *Photogrammetric Engineering and Remote Sensing*, 84 (10), 605-618.

Robinson, M.S., Brylow, S.M., Tschimmel, M., Humm, D., Lawrence, S.J., Thomas, P.C., Denevi, B.W., Bowman-Cisneros, E., Zerr, J., Ravine, M.A., 2010. Lunar reconnaissance orbiter camera (LROC) instrument overview. *Space Science Reviews*, 150 (1), 81-124.

Rothermel, M., Wenzel, K., Fritsch, D., Haala, N., 2012. Sure: Photogrammetric surface reconstruction from imagery. Proceedings LC3D Workshop, Berlin, Berlin, Germany.

Rupnik, E., Daakir, M., Deseilligny, M.P., 2017. MicMac–a free, open-source solution for photogrammetry. *Open Geospatial Data, Software and Standards*, 2 (1), 14.

Scharstein, D., Szeliski, R., 2002. A taxonomy and evaluation of dense two-frame stereo correspondence algorithms. *International Journal of Computer Vision*, 47 (1), 7-42.

Shean, D.E., Alexandrov, O., Moratto, Z.M., Smith, B.E., Joughin, I.R., Porter, C., Morin, P., 2016. An automated, open-source pipeline for mass production of digital elevation models (DEMs) from very-high-resolution commercial stereo satellite imagery. *ISPRS Journal of Photogrammetry and Remote Sensing*, 116, 101-117.

Tao, C.V., Hu, Y., 2002. 3D Reconstruction Methods based on the Rational Function Model. *Photogrammetric Engineering and Remote Sensing*, 68 (7), 705-714.

USGS, 2018. ISIS: Integrated Software for Imagers and Spectrometers, https://isis.astrogeology.usgs.gov/index.html. (28 June, 2018)

Wang, M., Hu, F., Li, J., 2011. Epipolar resampling of linear pushbroom satellite imagery by a new epipolarity model. *ISPRS Journal of Photogrammetry and Remote Sensing*, 66 (3), 347-355.

Wang, Y., Wu, B., 2017. Investigation of boresight offsets and co-registration of HiRISE and CTX imagery for precision Mars topographic mapping. *Planetary and Space Science*, 139, 18-30.

Wang, Z., 1990. Principle of Photogrammetry: with Remote Sensing. *Press of Wuhan Technical University of Surveying and Mapping*, Wuhan, 455.

Wu, B., Guo, J., Hu, H., Li, Z., Chen, Y., 2013. Co-registration of lunar topographic models derived from Chang'E-1, SELENE, and LRO laser altimeter data based on a novel surface matching method. *Earth and Planetary Science Letters*, 364, 68-84.

Wu, B., Hu, H., Guo, J., 2014. Integration of Chang'E-2 imagery and LRO laser altimeter data with a combined block adjustment for precision lunar topographic modeling. *Earth and Planetary Science Letters*, 391, 1-15.

Wu, B., Tang, S., Zhu, Q., Tong, K., Hu, H., Li, G., 2015. Geometric integration of high-resolution satellite imagery and airborne LiDAR data for improved geopositioning accuracy in metropolitan areas. *ISPRS Journal of Photogrammetry and Remote Sensing*, 109, 139-151.

Wu, B., Zhang, Y., Zhu, Q., 2011. A triangulation-based hierarchical image matching method for wide-baseline images. *Photogrammetric Engineering and Remote Sensing*, 77 (7), 695-708.

Wu, B. and Liu, W.C., 2017. Calibration of Boresight Offset of LROC NAC Imagery for Precision Lunar Topographic Mapping. *ISPRS Journal of Photogrammetry and Remote Sensing*, 128, 372–387.